



Published by Fusion Energy Division, Oak Ridge National Laboratory
Building 5700 P.O. Box 2008 Oak Ridge, TN 37831-6169, USA

Editor: James A. Rome

Issue 100

September 2005

E-Mail: jar@ornl.gov

Phone (865) 482-5643

On the Web at <http://www.ornl.gov/sci/fed/stelnews>

Stellarator News is 100!

The ORNL Fusion Energy Division joins the Editor of *Stellarator News*, James Rome, in marking the occasion of its 100th issue. Stellarators are three-dimensional magnetic confinement configurations. This extra degree of freedom results in a wide diversity of approaches that enrich our field of research and contribute to a better understanding of less complex systems such as the tokamak. *Stellarator News* was born in 1988 to equip our diverse and highly collaborative community with a communications tool that facilitates a rapid exchange of results and ideas. Published every other month, *Stellarator News* is edited but unrefereed, and can thus serve as a platform to promote new and possibly controversial ideas. *Stellarator News* publishes articles in theory, experiment, reactor design, and engineering, along with news and meeting proceedings.

The Fusion Energy Division has sponsored *Stellarator News* since its inception. We hope you, its readers, have found that it has served its purpose well. Finally, we salute Jim Rome for unselfishly bringing this service to us for nearly two decades.

Stanley L. Milora
Director, Fusion Energy Division
Oak Ridge National Laboratory

As Editor of *Stellarator News*, I would like to thank my hard-working contributors for providing the contents of each issue. I invite our readers to submit articles to me directly, or ask to be put on the contributor list. Being an electronic journal, *Stellarator News* has no page limits and encourages the use of color graphics.

I also thank Bonnie Nestor, the outstanding Technical Editor for *Stellarator News*. Bonnie knows the jargon of fusion better than many scientists, and is a stickler for clear and concise presentation of material. Bonnie has performed this task enthusiastically since the first issue.

James A. Rome, Editor

In this issue . . .

Magnetic flux surface measurements at Wendelstein W7-AS

The magnetic flux surfaces in W7-AS were remeasured and compared to the initial measurements from 1987; there were no significant changes. Surfaces were also measured at high magnetic field strengths to determine the effects of coil deformations. The three-dimensional topology near the magnetic surface was viewed using scattering on background gas. The magnetic field strength was measured using a new NMR technique. 2

Electron internal transport barriers, rationals, and quasi-coherent oscillations in the TJ-II stellarator

The evolution of core quasi-coherent modes has been investigated during the formation of electron internal transport barriers (e-ITBs) in the TJ-II stellarator. These modes have been characterized using heavy ion beam probe and electron cyclotron emission diagnostics. The quasi-coherent mode evolves during formation/annihilation of the e-ITB and vanishes as the transport barrier is fully developed. These observations can be interpreted in terms of the influence of sheared flows in the stability of quasi-coherent modes. 5

Neoclassical simulation of the geodesic acoustic mode with finite-orbit-width effects

A neoclassical transport code that includes finite-orbit-width effects was used to simulate the geodesic acoustic mode (GAM), the collisionless damping rate of GAM, and the time evolution of the radial electric field in tokamaks and helical model plasmas. The damping rate of the GAM oscillation is faster than that predicted from a previous neoclassical transport analysis. The result is consistent with a recent gyrokinetic study of the GAM which considers the finite-orbit-width effect. 8

All opinions expressed herein are those of the authors and should not be reproduced, quoted in publications, or used as a reference without the author's consent.

Oak Ridge National Laboratory is managed by UT-Battelle, LLC, for the U.S. Department of Energy.

Magnetic flux surface measurements at Wendelstein W7-AS

Vacuum magnetic flux surface measurements on Wendelstein W7-AS were made in 2004, after the end of plasma operation in July 2002. The main emphasis of these new measurements was to compare a few magnetic configurations sensitive to changes in rotational transform ι or island size with the initial measurements made in 1987 [1]. Also, different divertor configurations were studied using the additional island control coils installed for divertor plasma operation. The presence of the divertor considerably reduced the surface cross-section effective radius, to $r_{\text{eff}} \approx 16$ cm, compared to the original $r_{\text{eff}} \approx 21$ cm obtained without the divertor. The flux surface mappings were performed at a magnetic field strength $B_0 = 0.48$ T. For a few magnetic configurations, using only modular field (MF) and toroidal field (TF) coils, it was possible to extend the measurements to the operational magnetic field strength of $B_0 = 2.4$ T. The experimental results were compared with Werner's W7 field line tracing code [2].

The new flux surface measurements used the same fluorescent electron beam technique as the initial measurements. Using a directed electron beam parallel to the magnetic field vector and a fluorescent rod in the detection plane, the technique produces a Poincaré plot of the magnetic field lines. Measurements were made in the same triangular flux surface plane at $\varphi = 216^\circ$ used for the initial measurements. The single fluorescent detecting rod that was used, could be swept across the vessel cross-section in 20 s. The directed electron beam was created by a movable electron gun that was installed near the $\varphi = 144^\circ$ plane. The electrons emitted by a tungsten filament were accelerated in the electron gun to an energy of 100 eV with a beam intensity of ~ 10 μA . The measurements were made using a sensitive CCD camera with a long integration time. The camera was positioned almost perpendicular to the detector plane of the fluorescent rod, viewing through a tangential port. The measurements were performed under ultrahigh-vacuum conditions at a pressure below 3×10^{-7} mbar.

We also successfully applied new methods to make the magnetic field lines in the whole plasma vessel visible, and nuclear magnetic resonance (NMR) measurements to determine absolute magnetic field strength. All of the methods mentioned here will also be used on W7-X.

Magnetic field line mapping results

The magnetic coil system of W7-AS consists of a set of 45 nonplanar MF coils, 10 planar TF coils, a set of vertical field (VF) coils, and — during the divertor experiments — 10 control coils (CCs). In the standard configuration, where only the MF coils are used, the rotational transform ι is just under $2/5$ over the whole cross section, making small changes of ι easily detectable. A comparison of the new results with the initial measurements (Fig. 1) demonstrates that no serious discrepancies were detected.

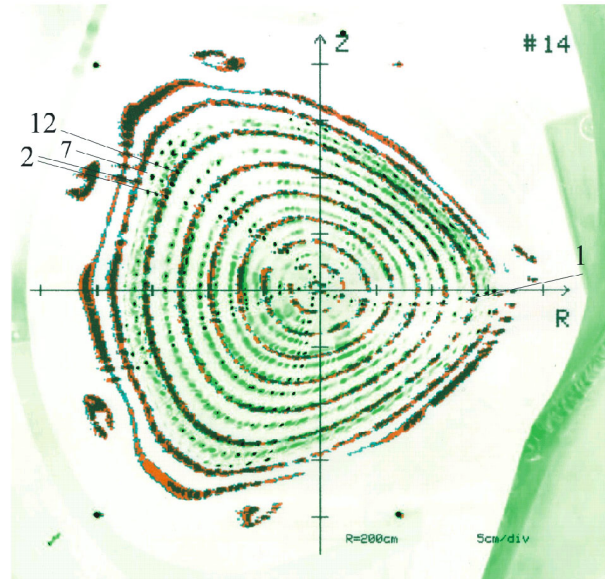


Fig. 1. Superposition of initial flux surface measurements (dark) with recent measurements (light, restricted cross section). The labels refer to the number of transits of the electron beam. The small gap between transits 2, 7, 12, etc., indicates that ι is just below 0.4.

The symmetry-breaking islands at $\iota = 2/5$ found in the initial experiments were not accessible in the new campaign because the plasma cross section was reduced by the divertor. However, the size of natural and symmetry-breaking magnetic islands was checked, and no significant changes were found. Furthermore, the position of the magnetic axis and the geometry of the magnetic flux surfaces were unchanged. Thus the shape of the MF coils is essentially unchanged after some 30,000 pulses at the full 2.5-T magnetic field, even though local deformations of the coils of up to 4 mm have been measured.

The high-current power supply used for the new measurements allowed extension of the Poincaré plot measurements to the full toroidal field of 2.5 T. Increased coil temperature limited the flat-top pulse length to 6 s in this case. However, this was sufficient to determine a change in ι with increased magnetic field. Because the magnetic forces have the tendency to flatten the nonplanar MF coils,

a decrease of ι was expected. As in Fig. 1, the first intersection points of a field line at $r_{\text{eff}} = 15.3$ cm were used for comparison. Figure 2 demonstrates an increasing poloidal spread of the intersection points with increasing toroidal field.

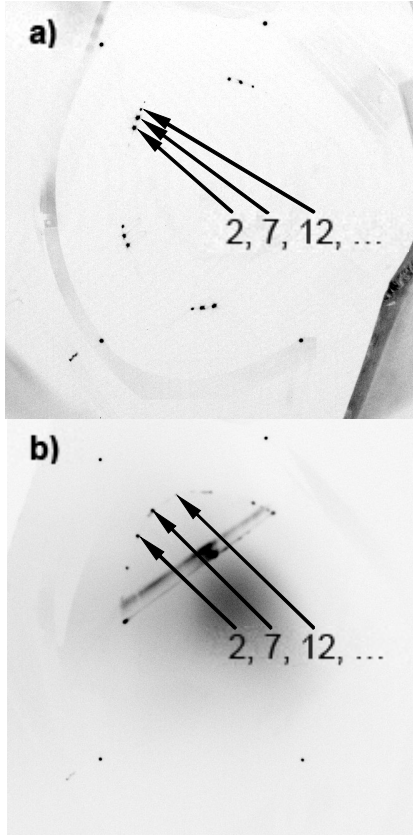


Fig. 2. Field line intersection points for the standard configuration at $r_{\text{eff}} = 15.3$ cm for (a) $B_0 = 0.48$ T and (b) $B_0 = 2.4$ T.

The W7 code was used to simulate this behavior and determine the rotational transform at higher magnetic fields. In the code, a small correcting field generated by the planar TF coils was added to the field produced by the MF coils. The correcting field component was varied so that the computed Poincaré plot best fit the measurements. The result, given in Fig. 3, shows a 2% decrease in ι at $r_{\text{eff}} = 15.3$ cm, from 0.3965 at $B_0 = 0.48$ T to 0.3894 at $B_0 = 2.42$ T.

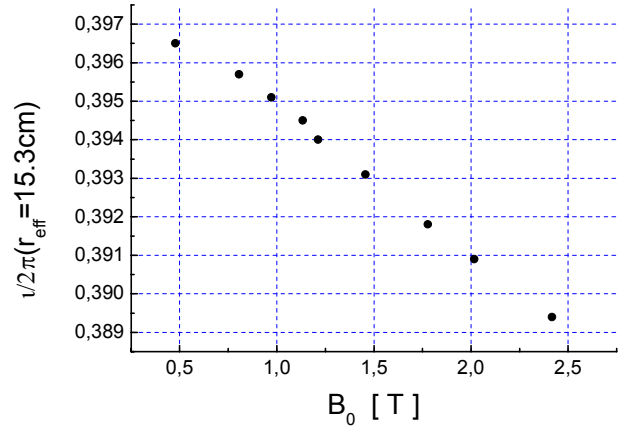


Fig. 3. Dependence of ι on the magnetic field strength for the standard configuration with MF coils only.

The unexpected almost linear behavior probably reflects the complicated mechanical boundary conditions that control the transfer of the magnetic forces into the support structure. The decrease of ι is fairly small, so that there is no need to modify the interpretation of the plasma experiments. The flux surface measurements at 2.5 T were also the first successful test of the fluorescent rod technique at high field, indicating that the technique can be used on W7-X at similarly high field strengths.

The CCs installed on W7-AS turned out to be an important tool for modifying the size of the natural 5/9 islands during the island divertor experiments. Therefore, the standard divertor magnetic field configuration was also mapped. In this configuration the TF and VF coils of W7-AS also had to be used, so that the magnetic field strength was limited to 0.5 T.

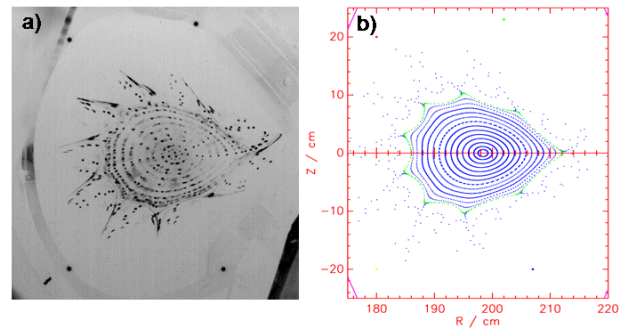


Fig. 4. (a) Experimental and (b) calculated flux surfaces of the standard divertor configuration with well-defined island fans and separatrix (green).

The results are presented in Fig. 4(a), where the magnetic separatrix and also part of the natural islands can be seen. The corresponding Poincaré plot, computed using the W7 code, shown in Fig. 4(b), is in good agreement with the measured results.

Visualization of magnetic field lines

Usually magnetic flux line mapping is restricted to one toroidal plane, so no information about nontoroidal symmetry is obtained. However, information on, for example, the position of the magnetic axis at various toroidal positions is frequently required for the interpretation of diagnostic signals. This information can be obtained rather easily if a magnetic field line close to the magnetic axis can be made “visible.”

Field line mapping is usually performed under ultrahigh-vacuum conditions in order to avoid diffusion of the electrons from their original drift surface owing to collisions with the residual gas. However, collisions with the background gas can also be used to obtain a visible trace of the electrons’ flight path along a magnetic field line because of inelastic collisional excitation of the neutrals [3, 4]. In contrast to the fluorescent electron beam mapping technique, only a manipulator with an electron gun is needed; a fluorescent detector is not required. After preliminary studies on the WEGA stellarator, the method was applied to W7-AS. Optimum conditions were found in hydrogen gas at a pressure of 3×10^{-5} mbar, an emission current of about 1 mA, and an electron accelerating voltage of 300 V. Using the same CCD camera used for the flux surface measurements, up to 35 toroidal turns could be detected, corresponding to a visible field line length of more than 400 m. The sample measurement in Fig. 5 shows a field line for $B_0 = 0.65$ T in the standard configuration with $\iota \leq 2/5$.

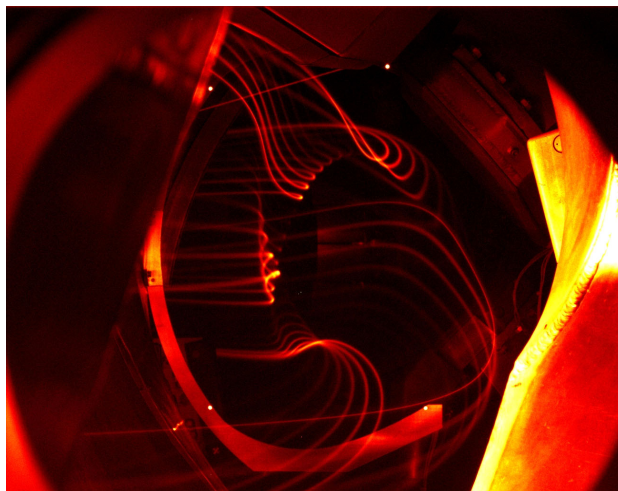


Fig. 5. Magnetic field line for $B_0 = 0.65$ T for the standard configuration with $\iota < 2/5$ in hydrogen gas (false colors).

For comparison with the flux surface results, measurements were made from low to high B_0 in the standard configuration. For a fixed position of the electron gun, the amplitude of the magnetic field strength was increased, shot by shot, to a field strength of 2.4 T. The increasing spread between successive transits (2, 7, 12, etc.) at higher B_0 , shown in Fig. 6, indicates qualitatively a decrease in rotational transform, as discussed above (see also Fig. 2).

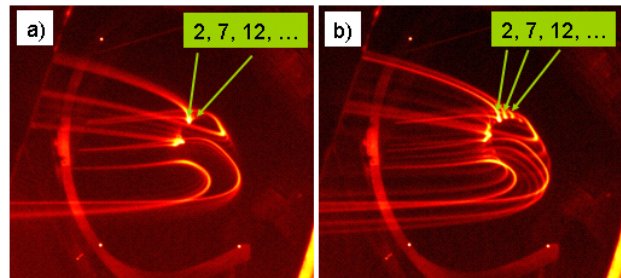


Fig. 6. Magnetic field line for (a) $B_0 = 0.79$ T and (b) $B_0 = 2.4$ T in hydrogen gas for the standard configuration (false colors).

For comparison with code calculations, the same field line tracing code used for the calculation of magnetic flux surfaces can be applied. Although the length of the visible trace is limited to a few hundred meters, the method can be used to determine the position of the magnetic axis and the X- and O-points and to check for changes in the rotational transform at higher fields. In W7-X, the mean circumference of a field line is about 35 m, so that at least 10 toroidal turns will be visible. A light-emitting field line can also be a useful calibration source for other diagnostics.

Measurements of absolute magnetic field strength

During plasma experiments on W7-AS, a discrepancy was often found between B_0 calculated from the coil currents and B_0 obtained from code calculations used to interpret diagnostic signals, for example, when electron cyclotron resonance was involved. Thus, an independent measure of the toroidal field strength was desired. NMR is a sensitive and direction-independent technique that can be used to measure the absolute value of B_0 . An NMR sensor, with maximum detectable field strength of 1.05 T, was used to measure B_0 in the same triangular plane in which the fluorescent rod was installed. At this toroidal position, the magnetic field strength B_0 near the magnetic axis is almost constant in the standard configuration, so position errors of the sensor and field gradients are negligible. It was found that the measured value of B_0 was about 0.5% smaller than the calculated value, possibly because of current ripple and interference. The range of values measured with the sensor was only about ± 0.2 mT, which is negligible.

M. Otte and R. Jaenicke
Max-Planck-Institut für Plasmaphysik
17491 Greifswald, Germany
E-mail: matthias.otte@ipp.mpg.de

References

- [1] R. Jaenicke et al., Nucl. Fusion, **11** (1993) 687.
- [2] A. Werner, private communication.
- [3] O. Neubauer et al., Fusion Technol. **31** (1997) 154.
- [4] T. S. Pedersen, *Stellarator News* 97 (2005) 1.

Electron internal transport barriers, rationals, and quasi-coherent oscillations in the TJ-II stellarator

Electron internal transport barriers (e-ITBs) are commonly observed in plasmas heated with electron cyclotron heating (ECH) in stellarator devices such as CHS [1], W7-AS [2], LHD [3], and TJ-II [4, 5].

In TJ-II, the formation of e-ITBs is triggered by positioning a low-order rational surface close to the plasma core region [4]. The key element that improves heat confinement is a locally strong positive electric field, which is the result of a synergistic effect between enhanced electron heat fluxes through radial positions around low-order rational surfaces and pump-out mechanisms in the heat deposition zone [5].

A recent improvement in the signal-to-noise ratio of the heavy ion beam probe (HIBP) system has allowed us to characterize the radial structure of plasma modes that appear during e-ITB formation in the core region of the TJ-II stellarator. The HIBP system installed at TJ-II uses a Cs^+ ion beam with beam energy of up to 200 keV [6]. The spatial resolution is about 1 cm. By sweeping the primary beam, the plasma potential can be measured in the whole plasma cross section with a repetition rate of a few milliseconds. Because of the relatively low plasma densities involved in these experiments ($0.5\text{--}1 \times 10^{19} \text{ m}^{-3}$), the secondary Cs^{++} beam intensity can be considered to be proportional to the local plasma density.

During e-ITB formation, the plasma potential increases in the plasma core region ($\rho < 0.3$), substantially increasing the radial electric field, while it remains almost unchanged at outer radii. Electron temperature as measured by the electron cyclotron emission (ECE) diagnostic also increases in the plasma core region. Quasi-coherent modes

with frequencies close to 20 kHz have been identified in the HIBP profiles during e-ITB formation. These modes are clearly observed in the beam current and, marginally, in the plasma potential. Figure 1(a) shows the radial profiles of the plasma potential and beam current measured by HIBP in a magnetic configuration having the rational surface $3/2$ close to the plasma core. The profiles are measured at two different time intervals during the discharge. The electron temperature profiles are shown in Fig. 1(b) and the frequency spectra of the HIBP signals are displayed in Figs. 1(c) and 1(d). The coherent mode is clearly seen in the secondary beam current signal measured at 1115 ms and appears also, though not so clearly, in the plasma potential. The mode appears in the plasma region where core $E_r \times B$ sheared flows develop during e-ITB formation. It is also observed that the formation of the barrier is accompanied by a strong reduction of the mode.

Experimentally, it is observed that the amplitude and the radial extension of the coherent modes evolve along a single discharge, and the modes are often observed in discharges in which the e-ITB has an intermittent behavior. The mode starts growing simultaneously with the decay in the central temperature, reaching its maximum amplitude and radial extension when the barrier is finally lost. The recovery of the barrier is accompanied by the vanishing of the mode. Figure 2 shows an example in which the e-ITB has an intermittent character during the first part of the discharge. A time expansion of four electron temperature signals is displayed in Fig. 2(b) and their frequency spectra are shown in Fig. 2(c). The mode appears first in the ECE channel located at $\rho \sim -0.35$; it then grows and expands to the adjacent channels reaching its maximum amplitude at $\rho \sim -0.24$.

HIBP measurements obtained at discrete radial positions in similar discharges show a maximum amplitude of the coherent mode at $|\rho| \sim 0.3$. A comparison between the ECE and the HIBP measurements is shown in Fig. 3. Experimental findings show a strong correlation between ECE and HIBP once the quasi-coherent mode is developed. The HIBP and ECE measurements allow us to conclude that the quasi-coherent modes are localized within the radial range $|\rho| = 0.0\text{--}0.4$, with maximum amplitude around $|\rho| = 0.25\text{--}0.35$, close to the foot of the e-ITB.

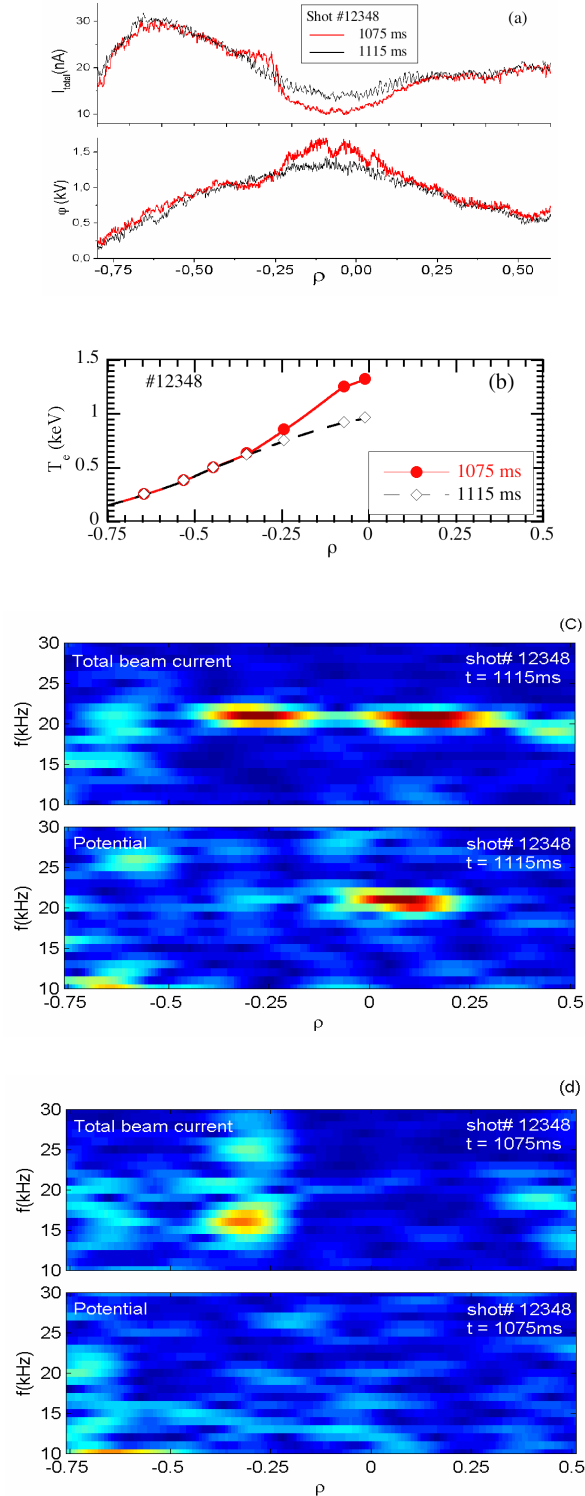


Fig. 1. (a) Profiles of plasma potential and beam current measured by HIBP at two different times of a discharge: without (black, 1115 ms) and with e-ITB (red, 1075 ms). (b) T_e profiles measured by ECE at the same times, and (c) spectra of beam current and plasma potential at 1115 ms. (d) Spectra of beam current and plasma potential at 1075 ms.

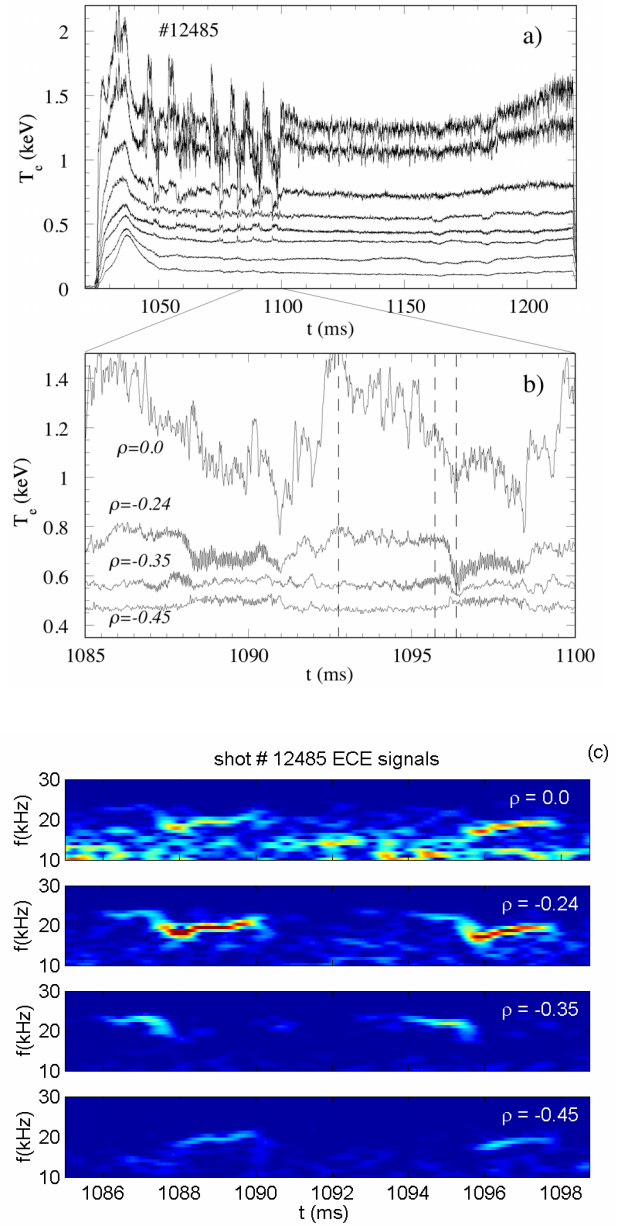


Fig. 2. (a) T_e in a plasma in which the e-ITB has an intermittent character during the first part of the discharge. Also shown are (b) time expansion and (c) spectra of four electron temperature signals.

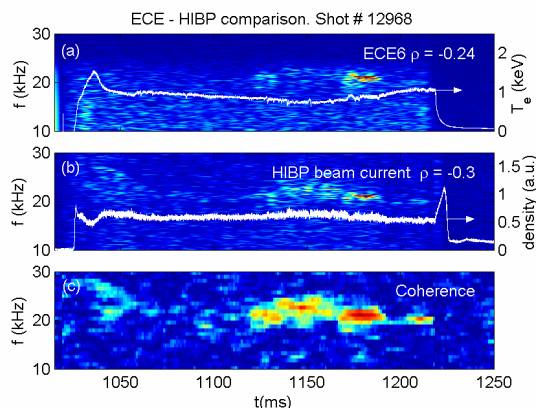


Fig. 3. Comparison of HIBP and ECE signals: (a) ECE evolution and spectrum at $\rho \sim -0.24$, (b) HIBP beam current evolution and spectrum at $\rho \sim -0.3$, and (c) coherence between the signals.

It is worth mentioning that though the presence of a low-order rational surface close to the plasma core is a necessary condition for triggering e-ITB formation in these experiments, the development of a quasi-coherent mode is not indispensable for the e-ITB formation. Many examples exist in which no coherent oscillation accompanies the formation of e-ITBs.

A possible cause of the reported quasi-coherent mode may be MHD instabilities. In this case, the radial electric field developed at the e-ITB formation may act as a stabilizing mechanism against the pressure gradient that should act as a free energy source. In the reported experiments, the quasi-coherent mode does not appear in the magnetic fluctuations measured by Mirnov coils. However, experiments in which the low-order rational is positioned at more external radii ($\rho = 0.6-0.8$) show a clear correlation between coherent oscillations measured by HIBP and Mirnov coils [7]. This difference could be a consequence of the localization of the mode at the plasma core, which may preclude its detection by the Mirnov coils. Alternatively, the lack of magnetic oscillations could also be an indication of a different mode origin. Taking into account the bifurcation characteristics of the e-ITB formation, there could be a critical point at which the competition between different mechanisms involved in the process produces an oscillatory behavior.

T. Estrada, A. Alonso, A. A. Chmyga,¹ N. Dreval,¹ L. Eliseev,²
C. Hidalgo, A. D. Komarov,¹ A. S. Kozachok,¹ L. Krupnik,¹
A. V. Melnikov,² I. S. Nedzelskiy,³ J. L. de Pablos, L. A. Pereira,³
Yu. Tashev,³ V. Tereshin,¹ I. Vargas
Laboratorio Nacional de Fusión
EURATOM-CIEMAT, 28040 Madrid, Spain
E-mail: teresa.estrada@ciemat.es

¹ Institute of Plasma Physics, NSC KIPT, 310108 Kharkov, Ukraine

² Institute of Nuclear Fusion, RNC Kurchatov Institute, Moscow, Russia

³ Associação EURATOM/IST, Centro de Fusão Nuclear, 1049-001 Lisboa, Portugal

References

- [1] A. Fujisawa et al., Phys. Rev. Lett. **82** (1999) 2669.
- [2] U. Stroth et al. Phys. Rev. Lett. **86** (2001) 5910.
- [3] T. Shimozuma et al., Plasma Phys. Control. Fusion **45** (2003) 1183.
- [4] T. Estrada et al., Plasma Phys. Control. Fusion **46** (2004) 277.
- [5] F. Castejón et al., Nucl. Fusion **44** (2004) 593.
- [6] A. Melnikov et al., Fusion Sci. Technol. **46** (2004) 299.
- [7] L. Krupnik et al., "Electron internal transport barriers, rationals, and fluctuations in TJ-II," paper P5.028, presented at the 32nd EPS Plasma Physics Conference, Tarragona, Spain, 2005 (to be published in the proceedings).

Neoclassical simulation of geodesic acoustic mode with finite-orbit-width effects

Zonal flows, the geodesic acoustic mode (GAM), and its collisionless damping have attracted much attention in recent theoretical and experimental studies. The GAM was first predicted by Winsor et al. [1] based on a fluid model, and kinetic evaluations of its frequency and the damping rate were done based either on the drift-kinetic equation [2, 3] or the gyrokinetic equation [4, 5]. Experimental observations of the GAM have been recently reported, for example in Ref. [6]. Recently, Sugama and Watanabe [7] showed from both gyrokinetic analysis and simulation that the collisionless GAM damping rate in tokamaks is considerably faster if the finite-orbit-width (FOW) effects of passing particles are considered. The FOW effect was neglected in the previous drift-kinetic, or neoclassical, treatment of the GAM.

Because the underlying physics of collisionless GAM damping is the same in both drift-kinetic and gyrokinetic treatments, the strong damping is also expected in a neoclassical simulation of the GAM if FOW effects are considered. On the other hand, in gyrokinetics, the background potential, which evolves so that the neoclassical transport satisfies the ambipolar condition, is usually neglected. In a real plasma, the total transport process consists of both short and long scale-length phenomena, which are treated separately by gyrokinetics and drift kinetics. However, analytical or even numerical investigation of the transport phenomena that embraces these two different scales is difficult. As a first step toward a comprehensive understanding of the GAM oscillation and zonal flows, detailed investigation of the damping phenomena of the GAM in based on gyrokinetics and drift-kinetics is required.

Recently, we have developed a global neoclassical transport simulation code using the δf method, named FORTEC-3D [8], which is applicable to both axisymmetric and non-axisymmetric geometries and includes FOW effects. By using FORTEC-3D, we investigate the GAM oscillation in the framework of drift kinetics[9]. It is found that the GAM damping rate is much faster than the collision time, as shown in the gyrokinetic simulation [7]. Here, we report several numerical results from our simulation.

Simulation model

In the δf method, the time development of the perturbation of the plasma distribution function from a local Maxwellian $\delta f = f - f_M$ is solved according to the drift-kinetic equation of the first order,

$$\begin{aligned} \frac{D\delta f}{Dt} &\equiv \frac{\partial \delta f}{\partial t} + (\mathbf{v}_{\parallel} + \mathbf{v}_d) \cdot \nabla \delta f + \mathcal{Z} \frac{\partial \delta f}{\partial \mathcal{Z}} - C_{\text{tp}}(\delta f) \\ &= -\mathbf{v}_d \cdot \nabla f_M - \mathcal{Z} \frac{\partial f_M}{\partial \mathcal{Z}} + \mathcal{P} f_M \end{aligned} \quad (1)$$

where $f_M(\rho, \mathcal{Z})$ is a local Maxwellian, $\mathcal{Z} = mv^2/2$, and \mathbf{v}_d is the drift velocity in the direction perpendicular to \mathbf{B} . The linearized Landau collision operator is decomposed into the test-particle part $C_{\text{tp}}(\delta f) = C(\delta f, f_M)$ and the field-particle part $\mathcal{P} f_M = C(f_M, \delta f)$. Note here that the term $\mathbf{v}_d \cdot \nabla \delta f$ in Eq. (1) brings in the FOW effect, which is neglected in standard neoclassical theory based on the small-orbit-width limit approximation. We adopted the two-weight scheme [10, 11] to solve Eq. (1) by a Monte Carlo method.

The time evolution of the radial electric field is evaluated from the radial neoclassical current as follows:

$$\varepsilon_0 \left[\langle |\nabla \rho|^2 \rangle + \left\langle \frac{c^2}{v_A^2} |\nabla \rho|^2 \right\rangle \right] \frac{\partial E_\rho}{\partial t} = e |\Gamma_i - \Gamma_e|, \quad (2)$$

where $\langle \dots \rangle$ indicates the flux-surface average, v_A is the Alfvén velocity, and the neoclassical particle flux is given by $\Gamma_a = \langle \int d^3v \dot{\rho} \delta f_a \rangle$. According to Eq. (2), the radial electric field evolves so that it satisfies the ambipolar condition $\Gamma_i = \Gamma_e$. In tokamak cases, the nonambipolar flux is mainly due to the FOW effect on ion transport, and therefore the small contribution from $\Gamma_e \sim O(\sqrt{m_e/m_i})\Gamma_i$ can be neglected. In non-axisymmetric cases, however, Γ_e is comparable to Γ_i and is needed to solve Eq. (2). Since the FOW effect is expected to be important mainly for ions, only the ion part of the drift-kinetic equation is solved in FORTEC-3D. To evaluate Γ_e , we use GSRAKE [12], a numerical solver of the ripple-averaged kinetic equation in helical systems. By using GSRAKE, the table of $\Gamma_e(\psi, E_\rho)$ in the entire simulation domain (ψ, E_ρ) is prepared, and the Γ_e -table is referenced at each step in FORTEC-3D to evaluate Eq. (2).

Simulation of GAM oscillation

We consider first a circular cross-section tokamak configuration. The major axis is $R_0 = 4$ m and the minor radius of the last closed flux surface (LCFS) is $a = 1$ m. The magnetic field on the axis is set to $B_0 = 2$ T or 4 T to observe the FOW effect by changing the radial deviation width of drift orbits. Density and temperature profiles have exponential slopes, and the central values are $n_0 = 2.5 \times 10^{19} \text{ m}^{-3}$ and $T_0 = 3$ keV, respectively. The reversed-shear safety factor (q) profile is used here to see the dependence of the GAM damping rate on the q profile. The effective collision frequency $\nu_i^* = qR_0/(\tau_i \nu_{\text{th}} \varepsilon^{3/2})$ is much smaller than unity over almost the whole plasma region, and collisional damping of GAM is not expected to be effective. In the simulations we used 38 million mark-

ers, and for evaluating the radial particle flux and electric field, we prepared 80 meshes in the ρ direction so that fine structure of E_ρ on the scale comparable to a banana width can be observed. The initial condition is chosen as $\delta f(t=0) = 0$ and $E_\rho(\rho, t=0) = 0$.

In Fig. 1, the time evolution of the radial electric field E_r at $\rho = 0.2, 0.5$, and 0.85 is shown. The safety factor on these surfaces correspond to 2.5, 1.1, and 4.5, respectively. For $\rho = 0.5$, strong damping of the GAM occurs. This is because of Landau damping at the $q \approx 1$ surface, where the resonance condition of the GAM and thermal passing particles is satisfied. In the previous simulation by Novakovskii, the damping rate of GAM is quite slow, $\gamma_{\text{GAM}} \sim v_i/q$, if $q \gg 1$. However, in our simulation the damping rate γ_{GAM} on the $\rho = 0.2$ and 0.85 surfaces, where $q \gg 1$, is much larger than τ_i^{-1} . Therefore, it is expected that a mechanism exists to strengthen the collisionless damping of the GAM and that it is effective even if $q \gg 1$. We expect that this is because of a FOW effect that is included in our simulation model.

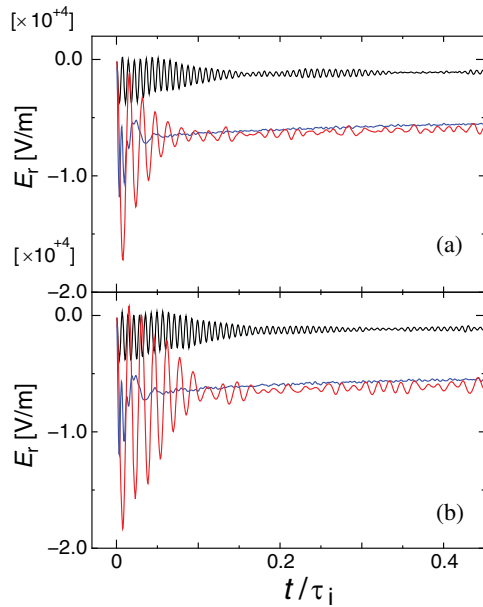


Fig. 1. The time evolution of radial electric field in reversed- q profile tokamak. Black, blue, and red lines represent E_r on three radial positions $\rho = 0.25, 0.5$, and 0.85 , respectively. $B_0 = 2\text{ T}$ in (a) and 4 T in (b).

Recently, Sugama and Watanabe [7] have analyzed the collisionless damping rate of the GAM in gyrokinetics, including the FOW effect of passing particles. In the small-orbit-width limit, as in the previous drift-kinetic studies, only the resonance of passing ions with the GAM at $|v_{\parallel}| = R_0 q \omega$ is effective in the collisionless GAM damping. They found that, if the FOW effect is taken into

account, the resonance at $|v_{\parallel}| = R_0 q \omega / 2$ becomes effective and γ_{GAM} becomes larger. This modification of γ_{GAM} disappears at the small-orbit-width limit, $k_r \rho_i \rightarrow 0$, where k_r is the perpendicular wave number. From both gyrokinetic-Vlasov simulation and analytic solution of the dispersion relation of GAM which includes the FOW effect of passing particles, the GAM damping is found to be much faster than that evaluated in the $k_r \rho_i \rightarrow 0$ limit, even in the case where $q \gg 1$ and the factor $k_r \rho_i$ is as small as 0.1 or less. The underlying physics of collisionless damping in drift kinetics is the same as that in gyrokinetics, and we consider that the rapid damping of the GAM in our neoclassical simulation can also be explained by the FOW effect. The FOW effect on the damping rate can be determined by the time evolution of E_r on $\rho = 0.85$. As the gyrokinetic analysis predicts, the damping is slightly faster in the $B_0 = 2\text{ T}$ calculation [Fig. 1(a)], in which the drift width is larger, than in the 4 T case [Fig. 1(b)]. Though the damping rate γ_{GAM} observed in our global simulation differs from previous local transport analysis, we find good agreement if the GAM frequency observed in the simulation with the analytic expression $\omega_{\text{GAM}} = \sqrt{7/4} v_{\text{th}} / R_0$.

Next, the time evolution of E_r in a Large Helical Device (LHD) [13] configuration is shown in Fig. 2. In helical plasmas, the ambipolar condition $\Gamma_e(\rho, E_r) = \Gamma_i(\rho, E_r)$ sometimes has multiple roots [14]. In order to avoid the transition of the radial electric field and to exploit only GAM oscillation in the simulation, we choose a plasma profile so that only one root appears in the entire plasma region. The n and T profiles are defined in the same way as in tokamak cases where $n_0 = 2.0 \times 10^{18} \text{ m}^{-3}$ and $T_0 = 1 \text{ keV}$. For the simulation of LHD, 64 million markers were used.

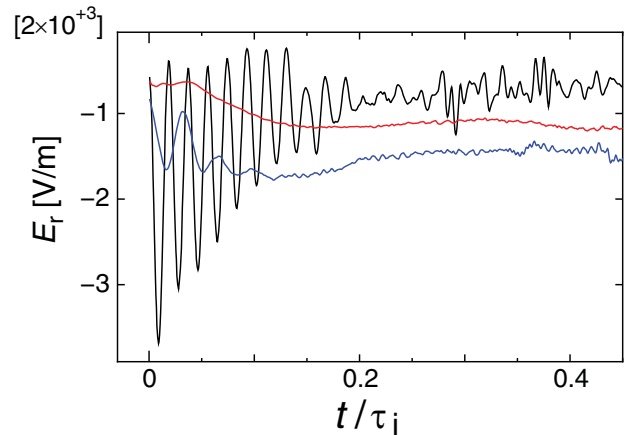


Fig. 2. The time evolution of radial electric field in a LHD configuration. Black, blue, and red lines represent E_r on three radial positions $\rho = 0.25, 0.5$, and 0.85 , respectively.

In considering GAM oscillation in the LHD configuration, we note that the rotational transform profile $\iota = 1/q$ is generally an increasing function of ρ . In the model configuration we use here, $\iota = 0.34$ on the magnetic axis and $\iota = 1$ at $\rho \sim 0.85$. It is found that in the outer region of plasma, $\rho > 0.5$, the GAM oscillation is strongly damped, and especially in the edge region, $\rho > 0.85$, in which the safety factor is < 1 , the GAM completely disappears. For the region where $q \gg 1$, γ_{GAM} at the inner surface, $\rho = 0.25$, is more rapid than the collision frequency τ_i^{-1} as is found in the tokamak cases. The GAM frequency in the LHD case is evaluated by taking the power spectrum of the E_r oscillation in Fig. 3. The frequency is slightly slower than the theoretical value for tokamaks, $\omega_{\text{GAM}} = \sqrt{7/4} v_{\text{th}} / R_0$. Though passing particle motion is considered to be responsible for determining the GAM oscillation frequency, helical components of the magnetic field spectrum perturb the passing particle motion. In the gyrokinetic analysis by Sugama and Watanabe for helical systems [15], a weak reduction of the frequency and strong damping of the GAM in the presence of helical ripples are theoretically predicted.

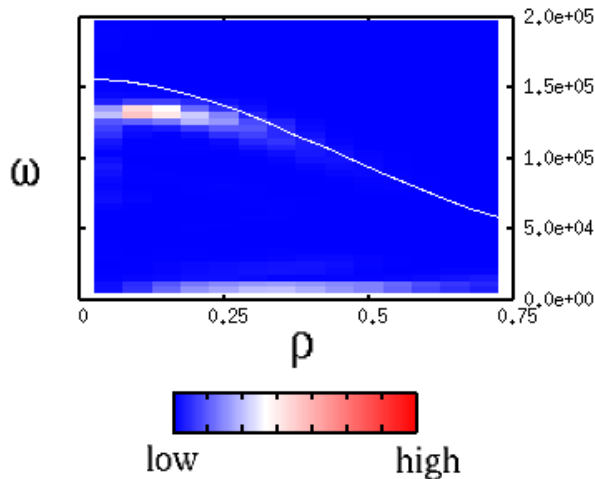


Fig. 3. Power spectrum of the radial electric field oscillation in the LHD case. Solid line represents the analytic value of the GAM frequency for tokamaks.

Concluding remarks

We have investigated the GAM oscillation and its collisionless damping by using a neoclassical transport code that includes the FOW effect. The damping rate is found to be larger than predicted by previous theory and numerical simulation based on the drift-kinetic equation, which does not consider the FOW effect. In a helical system, the GAM frequency is slightly lower than the theoretical value for tokamaks. These tendencies agree with the recent study of the effects of FOW and helical magnetic fields on the GAM based on gyrokinetics.

In helical systems, not only the FOW effect but also the helical components of the magnetic field spectrum will affect the GAM frequency and the damping rate. Recently, Watari et al. [16] derived the dispersion relation for the GAM in helical systems based on the drift-kinetic equation, though they do not consider the FOW effect. Now many theories about the GAM based on drift kinetics or gyrokinetics, in both tokamak and helical configurations, are available. Here, we have only qualitatively compared the numerical results with recent theories about the GAM damping rate. In the future, we plan to compare our simulation results with these theories, with the goal of revealing similarities and differences in the treatment of the GAM oscillation with gyrokinetics and drift-kinetics, and how the FOW effect acts on the GAM. The detailed understanding based on these two different views will help us to combine these two theories.

S. Satake, M. Okamoto, N. Nakajima, H. Sugama, and M. Yokoyama
National Institute for Fusion Science
322-6 Toki, Gifu, Japan
E-mail: satake.shinsuke@nifs.ac.jp

References

- [1] N. Winsor et al., Phys. Fluids **11** (1968) 2448.
- [2] V. B. Lebedev et al., Phys. Plasmas **3** (1996) 3023.
- [3] S. V. Novakovskii et al., Phys. Plasmas **4** (1997) 4272.
- [4] M. N. Rosenbluth and F. L. Hinton, Phys. Rev. Lett. **80** (1998) 724.
- [5] H. Sugama, and T.-H. Watanabe, Phys. Rev. Lett. **94** (2005) 115001.
- [6] A. Fujisawa et al., Phys. Rev. Lett. **93** (2004) 165002.
- [7] H. Sugama and T.-H. Watanabe, 19th International Conference on Numerical Simulation of Plasmas (2005); H. Sugama and T.-H. Watanabe, 7th Asia Pacific Plasma Theory Conference A6-2, submitted to J. Plasma Phys.
- [8] S. Satake et al., paper TH/P2-18 in Proceedings of 20th IAEA Fusion Energy Conference (2004).
- [9] S. Satake, "Non-local neoclassical transport simulation of geodesic acoustic mode," Nucl. Fusion, accepted for publication.
- [10] W. X. Wang, et al., Plasma Phys. Control. Fusion **41** (1999) 1091.
- [11] S. Brunner et al., Phys. Plasmas **6** (1999) 4504.
- [12] C. D. Beidler and W. D. D'haeseleer, Plasma Phys. Control. Fusion **37** (1995) 463.
- [13] A. Iiyoshi et al., Fusion Technol. **17** (1990) 169.
- [14] D. E. Hastings et al., Nucl. Fusion **25** (1985) 445.
- [15] H. Sugama and T.-H. Watanabe, to be submitted to Phys. Plasmas.
- [16] T. Watari et al., Phys. Plasmas **12** (2005) 062304.